Water Practice & Technology

IWA PUBLISHING

Water Practice & Technology Vol 19 No 3, 730 doi: 10.2166/wpt.2024.049

Facile removal of rhodamine B and metronidazole with mesoporous biochar prepared from palm tree biomass: adsorption studies, reusability, and mechanisms

Luqmon Azeez [a,*], Oyinlola Adefunke [a], Abdulrasaq O. Oyedeji [b], Babatunde K. Agbaogun [c], Hassan K. Busari [a], Ayoade L. Adejumo [d], Wasiu B. Agbaje [a], Adebayo E. Adeleke [e] and Awolola O. Samuel [a]

[a] Department of Pure and Applied Chemistry, Osun State University, Osogbom Trier, Nigeria
[b] Department of Science Laboratory Technology, Federal Polytechnic, Ilaro, Nigeria
[c] Analytical and Ecological Chemistry, University of Trier, Trier, Germany
[d] Department of Chemical Engineering, Osun State University, Osogbo, Nigeria
[e] Department of Basic Sciences, Adeleke University, Ede, Nigeria
*Corresponding author. E-mail: luqman.azeez@uniosun.edu.ng

LA, 0000-0002-6415-3490; AOO, 0000-0003-1592-3409; BKA, 0000-0002-5352-6108; HKB, 0000-0002-0440-3056; ALA, 0000-0002-1927-0209; WBA, 0000-0003-3719-9060; AEA, 0009-0005-7961-595X

ABSTRACT

Biochar was produced by pyrolysing palm tree bark biomass at 500 °C for the removal of rhodamine B (RhB) and metronidazole (MET). Fourier-transform infrared spectroscopy (FTIR), Brunauer–Emmett–Teller, X-ray diffraction (XRD), scanning electron microscopy, and energy-dispersive X-ray analyses were used to characterize the biochar. The biochar obtained was crystalline, mesoporous (SBET: 189.157 $m^2 g^{-1}$; pore diameter: 2.207 nm), clustered with prominent O–H and C = O functional groups. The pHpzc of the biochar was 7.98, and it adsorbed RhB and MET maximally at pH 3.4 and 7.2, respectively. The Langmuir and Freundlich isotherms described RhB and MET adsorption, respectively, with maximum adsorption capacities (q_{max}) of 31.81–224.30 mg/g for RhB and 95.44–26.76 mg/g for MET from 303 to 313 K. Both adsorbates exhibit favourable physisorption processes with pseudo-second-order kinetics, as the most appropriate. The thermodynamic parameter ($-\Delta G°$) demonstrates spontaneous adsorption processes for RhB and MET, with spontaneity increasing with temperature for RhB and decreasing with increasing temperature for MET. The adsorption process was endothermic ($+\Delta H°$) for RhB and exothermic ($-\Delta H°$) for MET. Given its reusability of 96 and 95% for RhB and MET, respectively, mesoporous biochar derived from palm trees is a more promising adsorbent.

Key words: crystalline biochar, mesoporosity, metronidazole, reusability, rhodamine B

HIGHLIGHTS

- Biochar was prepared from palm tree biomass and characterized to be mesoporous and crystalline.
- Adsorption of rhodamine B and metronidazole followed Langmuir and Freundlich isotherms, respectively.
- Adsorption capacities increased from 31.81 to 224.30 mg/g for RhB and decreased from 95.44 to 26.76 mg/g for MET with temperature.
- The kinetics of both adsorption processes followed pseudo-second order.
- Adsorption was spontaneous.

GRAPHICAL ABSTRACT

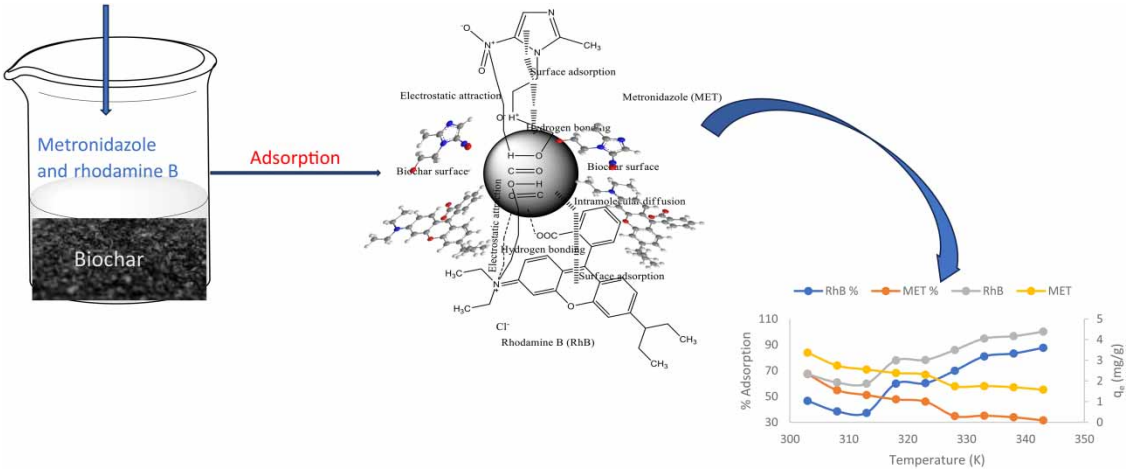

1. INTRODUCTION

Untreated toxic effluents are being released into the environment, especially into water sources, at an increasing rate due to urbanization and industrialization (Sarkhosh *et al.* 2019; Asgari *et al.* 2020; Akbari & Adibzadeh 2022). In view of the fact that industrial wastewater contains high levels of toxic, carcinogenic, and mutagenic pollutants, it is crucial that these pollutants be removed before being released into the environment (Duan *et al.* 2020; Azeez *et al.* 2022, 2023). Rhodamine B and metronidazole are pollutants found in surface and groundwater. They originate majorly from industries, such as paper and pulp, textiles, leather, and pharmaceuticals. Rhodamine B is a persistent dye while metronidazole is an emerging contaminant (Azeez *et al.* 2020; Ahmadfazelia *et al.* 2021; Bingül 2022).

Rhodamine B (RhB) is a light-resistant, heat-stable synthetic cationic dye used in textiles and dietary products (Azeez *et al.* 2018; Li *et al.* 2018). RhB has been linked to skin irritation, pulmonary inflammation, haemolysis, liver and kidney degeneration, and similar disorders once it exceeds the maximum acceptable concentration (tolerance limit) of 140 μgL^{-1} (Albanio *et al.* 2021; da Silva *et al.* 2022; Li *et al.* 2022; Sharma *et al.* 2022; Zhou *et al.* 2022). Due to the aromatic rings in the RhB structure, it is difficult to degrade. Its pollution of water and accumulation in aquatic organisms have increased as a result (Sridhar *et al.* 2022; Usman & Khan 2022; Li *et al.* 2023).

Metronidazole (MET) is an imidazole antibiotic that treats bacterial and protozoal infections in humans and animals. Due to its wide use and high solubility in water, it accumulates in aquatic environments (Nasseh *et al.* 2019; Asgari *et al.* 2020; Ahmadfazelia *et al.* 2021). It has been reported to cause cancer and mutations in humans as well as damage to the brain, lymph, and blood, especially when the tolerance limit of 171.54 ng mL^{-1} is exceeded (Hanna *et al.* 2018; Li *et al.* 2019; Bonyadi *et al.* 2021; Esmaili *et al.* 2023).

In developing countries such as Nigeria, there is no legislation regulating the concentration of RhB and MET in wastewater at present. Nonetheless, RhB and MET levels as low as 140 $\mu g\ L^{-1}$ and 10 ng/L make aquatic environments unsuitable for animals, while lethal levels between 14 and 24 mg/L RhB and between 11 and 13 ng/mL MET could cause 50% toxicity to animals as previously reported (Nasseh *et al.* 2019; Ahmadfazelia *et al.* 2021; Sridhar *et al.* 2022; Usman & Khan 2022; Li *et al.* 2023).

The continuous release of pollutants into water bodies has made clean water increasingly difficult to obtain. As well, a lack of proper regulation on effluent disposal and improper treatment may adversely affect Sustainable Development Goals (SDG 6) (clean water and sanitation) (Mukherjee *et al.* 2023a, 2023b).

The most effective, efficient, and safest method of dealing with emerging pollutants is adsorption due to its superiority to other treatment methods including its efficiency, convenience, simplicity, and cost-effectiveness (Albanio *et al.* 2021; Le *et al.* 2021; da Silva *et al.* 2022; Li *et al.* 2022, 2023; Azeez *et al.* 2023). However, commercially available adsorbents are usually expensive to purchase while agriculture continually generates large amounts of biomass that can cause environmental and ecological challenges if not properly disposed of (Adeniyi *et al.* 2019; Vigneshwaran *et al.* 2021; Zhang *et al.* 2021; Li *et al.* 2022; Zhou *et al.* 2022; Burezq & Davidson 2023). It is, therefore, necessary to recycle agricultural biomass and rid the environment of waste. Biochar can

be made from biomass due to its high lignin, hemicellulose, and cellulose contents (Burezq & Davidson 2023). The use of agricultural biomass for biochar production can be beneficial for waste management, climate change mitigation, and soil amendment (Vigneshwaran *et al.* 2021). A variety of materials have been used to produce biochar including rice husk, Chinese medicine herb residues, cement waste, coconut shell, rice bran, sugarcane bagasse, olive biomass waste, and date palm residue (Adeniyi *et al.* 2019; Albanio *et al.* 2021; Le *et al.* 2021; Vigneshwaran *et al.* 2021; Zhang *et al.* 2021; da Silva *et al.* 2022; Li *et al.* 2022; Burezq & Davidson 2023). Biochar is produced by pyrolysis of biomass under oxygen-limited conditions and has many benefits, including renewability, biodegradability, regeneration, and high porosity with a large surface area. Biochar's cost-effectiveness, availability, and ease of preparation make it an appealing adsorbent for wastewater treatment (Adeniyi *et al.* 2019; Olorunfemi *et al.* 2019; Yaashikaaa *et al.* 2019; Vigneshwaran *et al.* 2021). The threat of these pollutants to aquatic environments and human health has been demonstrated both individually and jointly, this study investigated the adsorption of RhB and MET on biochar made from palm tree bark to achieve environmental sustainability by converting waste biomass into useful biochar with minimal combustion and ash content and maximum carbon content.

2. MATERIALS AND METHODS

2.1. Biochar production and characterization

Palm tree bark was collected from a farm in Ilesa, Osun State, Nigeria. The bark was sun-dried for 24 h and then ground using a Eurosonic blender (Nigeria). The pulverized palm tree bark was pyrolysed in the muffle furnace at 500 °C peak for 5 h and cooled for 2 h following the method of Salem *et al.* (2021). Biochar functional groups were determined using a Fourier-transform infrared (FTIR) spectrometer (Shimadzu FTIR 8400S, Japan) by scanning from 400 to 4,000 cm^{-1}. In addition, scanning electron microscopy (SEM Phenom PRO X, Phenom world BV, Netherlands) was used to analyse morphological parameters, and energy-dispersive X-ray fluorescence was used to determine the surface elemental composition of biochar (EDXRF ARL XTRA Thermoscientific, Switzerland). In addition, an X-ray diffractometer (XRD Thermofisher, Switzerland) was used to ascertain the crystallinity and particle size was calculated using Debye–Scherrer formula (Equation (1)). The surface area, porosity, and shape of the isotherm were determined using Brunauer–Emmett–Teller (BET, Quantachrome Autosorb 1 series, USA).

$$D = \frac{0.94\lambda}{\beta Cos\theta} \tag{1}$$

where D is the particle size, λ is the wavelength of X-ray, β is the full-width half maximum, and θ is the diffraction angle.

2.2. Reagents and adsorbate characteristics

Rhodamine B (98%), metronidazole (99.5%), NaOH (99.5%), HCl (99%), and CH_3CH_2OH (99.5%) are analar grade reagents purchased from Sigma-Aldrich, Germany. A UV–Visible spectrometer was used to confirm the purity of RhB and MET purchased. Their maximum absorption was found to be at 555 and 320 nm, respectively, as previously reported (Ahmadfazelia *et al.* 2021; Azeez *et al.* 2022).

2.3. pH point of zero charge (pH_{pzc})

To measure the pH point of zero charge (pH_{pzc}), the pH of 0.1 g of mesoporous biochar in 0.1 M NaCl solution was adjusted from 1 to 12 using 0.1 M HCl/NaOH at room temperature. The pH_{pzc} was calculated by measuring the final pH after 24 h and extrapolating from the point of intersection in the plot of the final pH against the initial pH. A Jenway 3,505 pH meter was used to measure pH.

2.4. Adsorption studies of rhodamine B and metronidazole

The influence of the initial pH of RhB/MET solution (2–11), contact time (10–200 min), biochar dosage (0.1–0.5 g), and initial RhB/MET concentration (10–50 mg/L) on the adsorption of RhB/MET onto biochar was investigated. The working solutions of RhB and MET were adjusted to the desired pH values with 0.1 M HCl/NaOH. In a 100 mL conical flask, 0.5 g biochar was added to 50 mL of 50 mg/L RhB solution. A thermostatically controlled water bath shaker (Uniscope water bath shaker) was used to agitate the flask at 1,500 rpm for 100 min at 30 °C. The same procedure was repeated for MET. A Jenway 6405 UV–Visible spectrophotometer (Buch

Scientific Inc., USA) was used to measure the residual RhB and MET concentrations at 555 and 320 nm, respectively. Equations (2) and (3) were used to calculate the percentage removal and quantity adsorbed per gram of biochar.

$$\text{RhB/MET removal (\%)} = \frac{C_\text{i} - C_\text{f}}{C_\text{i}} \times 100 \tag{2}$$

$$q_\text{e} = \frac{(C_i - C_t)V}{M} \tag{3}$$

where q_e is the amount of RhB/MET adsorbed per biochar gram (mg/g); C_t, C_i, and C_f are residual, initial, and final RhB/MET concentrations (mg/L); V is the volume of RhB/MET solution (L); M is the biochar mass (g).

2.5. Adsorption isotherms, kinetics, and thermodynamics of RhB and MET

Adsorption data were described using Langmuir, Freundlich, Temkin, and Dubinin–Radushkevich isotherm models (Table 2) while adsorption kinetics were described with pseudo-first-order (PFO), pseudo-second-order (PSO), Elovich, and intra-particle diffusion model equations (Table 3). These models are required to explain adsorption isotherms and kinetics of adsorbates for preference on homogenous or heterogeneous surfaces of adsorbents, and the distribution of energy levels relative to their removal kinetics. Thermodynamic parameters obtained from Van't Hoff's equations (Table 5) were used to explain the energetics and spontaneity of the adsorption process for the removal of RhB/MET from mesoporous biochar produced from palm tree biomass. The best model was determined by root mean square error (RMSE, Equation (4)), Chi-square (χ^2, Equation (5)), and coefficient of determination (R^2, Equation (6)).

$$\text{RMSE} = \sqrt{\frac{1}{n-2}\sum_{i=1}^{n}(q_\text{e,means} - q_\text{e,cal})^2} \tag{4}$$

$$\chi^2 = \sum_{i=1}^{n}\frac{(q_\text{exp} - q_\text{cal})^2}{q_\text{cal}} \tag{5}$$

$$R^2 = \left(\frac{\sum(x_i - \bar{x})(y_i - \bar{y})}{\sqrt{\sum(x_i - \bar{x})^2(y_i - \bar{y})^2}}\right)^2 \tag{6}$$

where x denotes the q_e of each model and y denotes the experimental q_e.

2.6. Reusability and desorption study

This experiment examined biochar regeneration/reusability following its initial use for RhB/MET removal in ethanol and water. Briefly, 0.1 g biochar was added to 25 mL of 50 mg L^{-1} RhB and MET, with their pH adjusted to 3.4 and 7.2 (the maximum adsorption pH) and stirred at 303 K for 1 h before centrifuging at 300 rpm. After centrifugation, desorption was carried out with deionized-distilled water and ethanol, and the residual concentration of RhB/MET was determined. Three additional cycles were done. The reusability/desorption percentage was calculated using the following equation.

$$\text{Percentage desorption} = \frac{\text{quantity of RhB/MET desorbed in water/ethanol}}{\text{quantity of RhB/MET desorbed after loading}} \times 100 \tag{7}$$

3. RESULTS AND DISCUSSION

3.1. Characterization of biochar produced from palm trees

FTIR spectrum of biochar showed distinct peaks at 3,441 cm^{-1} attributable to the stretching O–H possibly from carboxyl, phenol, and alcohol functional groups. The peaks at 1,684, 1,559, and 1,653 cm^{-1} correspond to the C = O of conjugated ketone, carboxylic acid and C = C groups, respectively (Figure 1). The peak at 1,111 cm^{-1} is assigned to the C–O of alcohol. This result is consistent with previously reported FTIR spectra of biochar

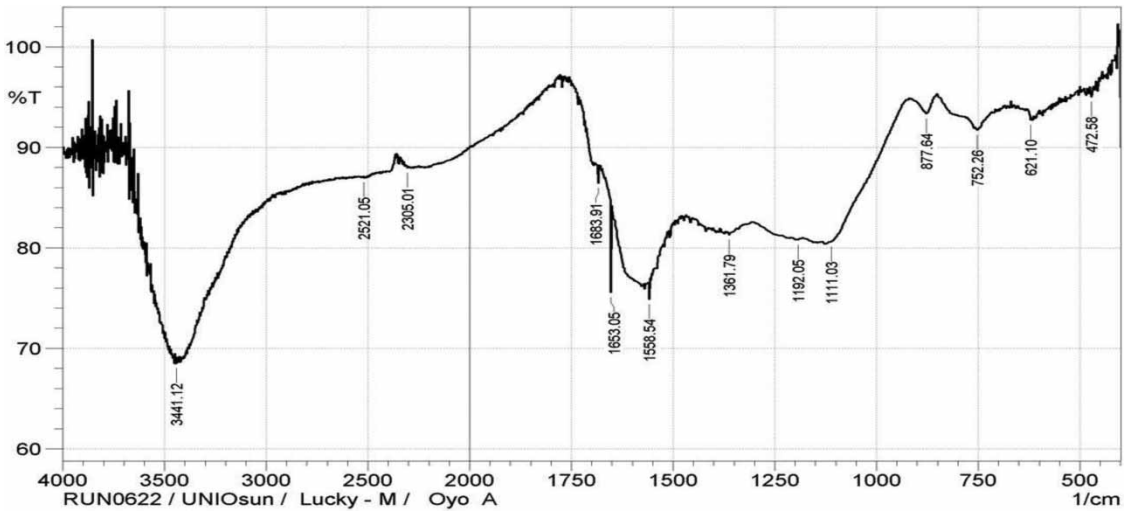

Figure 1 | FTIR spectrum of biochar produced from palm tree bark.

produced from rice rusk, Chinese herb medicine residue, and sugarcane bagasse (Li *et al.* 2019, 2022, 2023; Albanio *et al.* 2021; Le *et al.* 2021; Zhang *et al.* 2021).

According to the SEM micrograph (Figure S1a; supplementary document), the biochar is primarily oval-shaped with some cylindrical areas and amorphous with rough edges containing C, K, Cl, Ca, Fe, Ni, Cu, and Zn as revealed by the EDXRF analysis (Figure S1b; supplementary document). The SEM micrograph showed cavities that would favour the adsorption of pollutants. Usually, the elemental composition of biochar depends on its source (da Silva *et al.* 2022; Li *et al.* 2022).

X-ray diffraction (XRD) analysis of biochar revealed monoclinic-shaped particles with an average particle size of 34.21 nm and an average interplanar spacing of 2.172, matching Joint Committee on Powder Diffraction Standard (JCPDS) card number 00-712-6280 (Figure 2). The lattice parameters are $a = 31.0593$ Å, $c = 21.8198$ Å with six notable diffraction peak angles at $2\theta = 28.41°$, 40.57°, 50.24°, 58.71°, 66.45°, and 73.77°. These peaks correspond to hkl crystal planes of (111), (102), (110), (200), (112), and (202). This aligns with the report of Albanio *et al.* (2021).

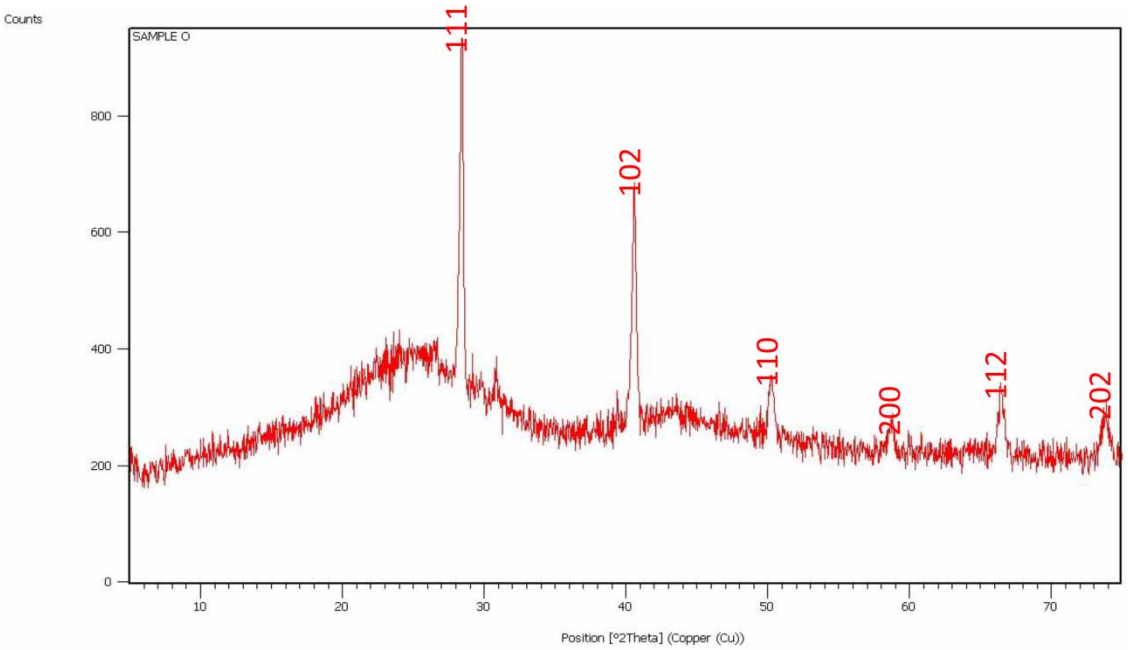

Figure 2 | XRD of biochar produced from palm tree bark.

A type II isotherm (Figure S2a; supplementary document), N_2 adsorption/desorption cycle with H4 hysteresis (Figure S2b; supplementary document), and mesoporous pore diameter distribution (Figure S2c; supplementary document) were determined with BET at 77 K. These results suggest a mesoporous material with macroporous slits that could be useful for unrestricted monolayer adsorption or multilayer adsorption. The S_{BET}, total pore volume, average pore diameter, and micropore surface area (Table 1) indicate a mesoporous biochar, with an average pore diameter of 2.207 nm appearing within a range of 2–50 nm (Li *et al.* 2022, 2023; Azeez *et al.* 2023).

Table 1 | Textural properties of biochar produced from palm tree

BET surface area ($m^2\ g^{-1}$)	189.157
Micropore surface area ($m^2\ g^{-1}$)	189.318
Barret-Joyner-Halenda (BJH) total pore volume (cc g^{-1})	0.097
BJH average pore diameter (nm)	2.207

3.2. pH point of zero charge (pH_{pzc})

The mesoporous biochar had a pH_{pzc} of 7.98 (Figure 3), which implies that its surface was positively charged and attracting anions below pH_{pzc}, and negatively charged and attracting cations above pH_{pzc} (Azeez *et al.* 2020, 2022; Ren *et al.* 2020; Bonyadi *et al.* 2021). The surface functionality of the biochar, as represented by pH_{pzc}, determines the strength of attraction between it and RhB/MET, which depends on functional groups, cavities, and electrostatic interaction between the adsorbent and adsorbate (Sridhar *et al.* 2022; Zhou *et al.* 2022; Nayak *et al.* 2023).

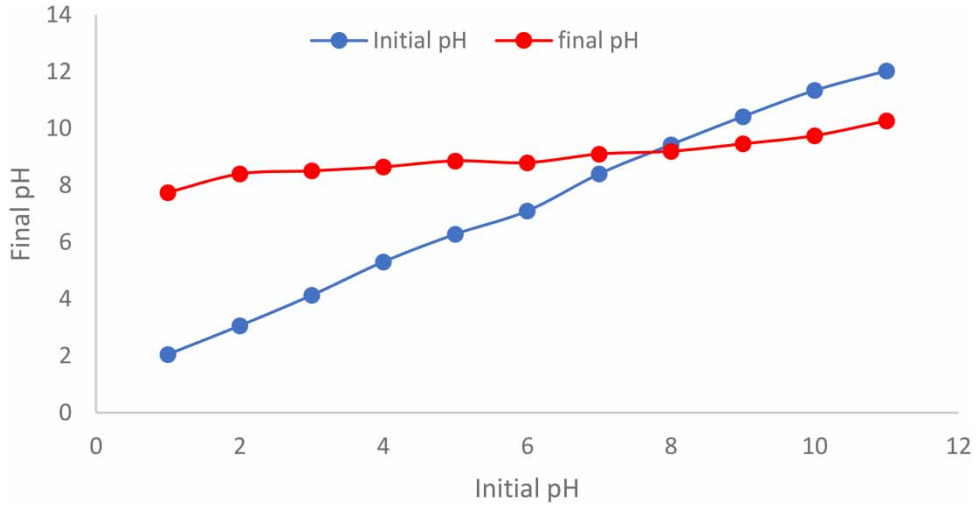

Figure 3 | pH point of zero charge (pH_{pzc}) of biochar produced from palm tree bark.

3.3. Influence of pH on RhB and MET adsorption

pH changes may either decrease or increase the adsorption percentage, depending on the surface charge of an adsorbent and mobility of the adsorbate (Elsayed *et al.* 2022; Liu *et al.* 2022). RhB removal increased from 90 to 93% with pH from 2 to 3.4 (Figure S3; supplementary document) and decreased to the minimum (45%) at pH 9. RhB exists in three forms; two as cationic RhB at $pH < 1$ as $RhBH_2^{2+}$, and between pH 1 and 3 as $RhBH^+$. The zwitterionic form ($RhB^{\pm}$) exists at $pH > 4$ where the positive and negative charges are located in $=N^+$ and COO^-. The electrostatic interaction between biochar and RhB at pH 3.4, where maximum adsorption occurred, is thus greatly impacted by electron transfer from COO^- of RhB to mesoporous biochar surface due to its cationic surface charge at this pH (Azeez *et al.* 2018, 2020, 2023; da Silva *et al.* 2022; Liu *et al.* 2022; Zhou *et al.* 2022). As the pH increased, biochar surface became less cationic as it approached its pH_{pz}, and then anionic above it leading to repulsion between RhB and biochar, thus low percentage adsorption. The

percentage removal of MET increased from 62 to 96% when the pH was increased from 5 to 7.2 with sinusoidal adsorption percentages. This is consistent with results of MET adsorption on biomass-derived porous aminated graphitic nanosheets with maximum adsorption at pH 8 (Bonyadi *et al.* 2021). Metronidazole (MET) has two pK_a values ($pK_{a1} = 2.38$ and $pK_{a2} = 14.48$). It exists as a protonated species (MET-H^+) at pH < 4, owing to the positively charged imidazoline nitrogen. Between pH 4 and 12, MET exists as a neutral species due to deprotonated imidazoline nitrogen while at pH > 12 the OH in MET is ionized, resulting in a negatively charged MET^- species (Ahmadfazelia *et al.* 2021; Bonyadi *et al.* 2021; Esmaili *et al.* 2023; Nayak *et al.* 2023). Thus, MET adsorption at this pH involved π–π interaction and electrostatic attraction between MET OH and biochar as well as hydrogen bonding interactions between the MET ring and cationic surfaces of the adsorbent (Vasseghian *et al.* 2022; Ghosh *et al.* 2023; Haghighat *et al.* 2023). RhB and MET adsorption per unit gram of biochar (q_e, Figure S3) follow a similar pattern as percentage adsorption.

3.4. Influence of adsorbent dosage

An assessment of the influence of mesoporous biochar dosage on RhB and MET removal (Figure S4; supplementary document) shows a dosage-dependent increase for RhB removal while a sinusoidal increase was obtained for MET. As the biochar dosage increased from 0.1 to 0.5 g, RhB adsorption increased from 49 to 74% while MET adsorption rose from 8 to 89%. Moreover, the quantity of RhB/MET adsorbed per gram of biochar (q_e, Figure S4) follows a similar trend, with RhB adsorption increasing from 0.022 to 0.248 mg/g and MET adsorption increasing from 0.132 to 0.199 mg/g. This increase could be attributed to an availability of more binding sites for the adsorbates. Similar results have been reported by Ahmadfazelia *et al.* (2021) and Esmaili *et al.* (2023).

3.5. Influence of initial RhB/MET concentrations and adsorption isotherms

The results of the influence of initial RhB/MET concentrations at different temperatures on the percentage uptake of RhB and MET on mesoporous biochar (Figure 4) showed that the percentage removal of RhB and MET decreased with increasing concentration of the adsorbates whereas the amount adsorbed (q_e) increased with increasing solute concentrations, as also previously reported by Azeez *et al.* (2018, 2023). Also, temperature variations significantly affected their removal correlating with higher adsorption for RhB and decreasing removal for MET as the temperature rose from 303 to 313 K. Possibly, the significant removal of RhB/MET at the beginning can be explained by the interaction between both adsorbates and the surface of mesoporous biochar at low initial concentrations (Vigneshwaran *et al.* 2021). As RhB/MET concentrations increased, fewer adsorption sites became available, resulting in RhB/MET molecules competing for adsorption sites, thus, the reduction (Ren *et al.* 2020; Vigneshwaran *et al.* 2021; Li *et al.* 2022, 2023). Azeez *et al.* (2018, 2023) reported previously that RhB adsorption increased with increasing concentrations due to higher concentrations. The combined effects of concentration and

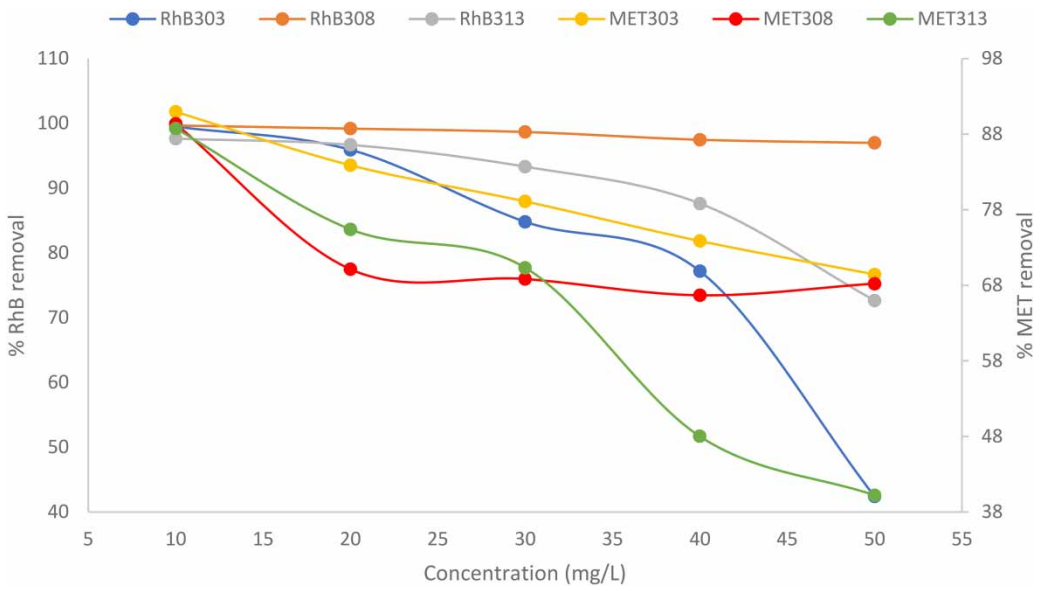

Figure 4 | Percentage adsorption of RhB and metronidazole (MET).

Table 2 | Isotherm models' parameters for the removal of RhB and MET at different temperatures on mesoporous biochar

			RhB			MET		
Isotherms	**Isothermal equations**	**Parameters**	**303 K**	**308 K**	**313 K**	**303 K**	**308 K**	**313 K**
Langmuir	$\frac{C_e}{q_e} = \frac{C_e}{q_{max}} + \frac{1}{q_{max}K_L}$	q_{max} (mg g^{-1})	31.81	173.12	224.30	95.44	46.65	26.76
		K_L (L mg^{-1})	127.24	217.22	118.45	0.03	0.28	0.10
	$R_L = \frac{1}{1 + K_L C_o}$	R_L	0.07	0.20	0.09	0.06	0.21	0.05
		R^2	0.990	0.988	0.991	0.691	0.687	0.931
		RMSE	0.013	0.002	0.001	4.476	3.923	0.325
Freundlich	$\log q_e = \frac{1}{n}\log C_e + \log K_f$	n	2.56	1.35	1.30	1.35	1.69	2.05
		K_f	2.30	2.30	4.34	4.17	3.89	3.54
		R^2	0.712	0.814	0.812	0.895	0.709	0.977
		RMSE	0.247	0.164	0.163	0.394	0.914	0.108
Temkin	$q_e = B\ln A + B\ln C_e$	B	2.265	7.642	7.064	8.667	7.192	5.105
	$B = \frac{RT}{b}$	A (L g^{-1})	1.849	1.503	0.677	1.289	1.039	1.429
		b (J mol^{-1})	1,112.12	329.63	356.58	290.63	350.26	493.42
		R^2	0.654	0.555	0.551	0.689	0.439	0.897
		RMSE	0.491	0.393	0.388	1.167	1.761	0.349
Dubinin–Radushkevich	$\ln q_e = \ln q_o - \beta\varepsilon^2$	q_o (mg g^{-1})	4.409	21.356	17.740	19.73	13.98	13.88
	$\varepsilon = RT\ln\left(1 + \frac{1}{C_e}\right)$	$\beta \times 10^{-7}$ (mol^2 kJ^{-2})	0.262	0.406	0.588	4.444	4.07	4.33
	$E = \sqrt{\frac{1}{2\beta}}$	E (kJ mol^{-1})	1.437	1.351	1.292	1.061	1.107	1.074
		R^2	0.350	0.728	0.722	0.610	0.450	0.652
		RMSE	0.558	0.240	0.241	1.461	1.724	1.173

RhB, rhodamine B; MET, metronidazole; C_e, dye equilibrium concentration (mg L^{-1}); q_e, the quantity of RhB/MET adsorbed (mg g^{-1}) per unit mass; q_{max}, maximum monolayer adsorption capacity (mg g^{-1}); K_L, Langmuir adsorption constant (L mg^{-1}); R_L, unitless constant for favourability; K_f, Freundlich constant; n, heterogenicity factor; B and E are the heat and energy of adsorption, respectively. R^2 and RMSE are the correlation coefficient and root square mean, respectively.

Table 3 | Comparison of adsorption capacity of RhB and MET on mesoporous biochar with previously published results

	RhB			**MET**		
	Adsorbent	**q_{max} (mgg^{-1})**	**Reference**	**Adsorbent**	**q_{max} (mgg^{-1})**	**Reference**
1	Hierarchically porous tobacco midrib-based biochar	658.2	Zhang *et al.* (2022)	AMGG (amine-modified green-graphene)	416.7	Bonyadi *et al.* (2021)
	Activated cement waste biochar	531.84	da Silva *et al.* (2022)	Fe_3O_4-chitosan nano adsorbent	97.06	Asgari *et al.* (2020)
	Olive biomass waste biochar	263.71	Albanio *et al.* (2021)	**Mesoporous palm tree biochar**	**95.44**	**This study**
	Mesoporous palm tree biochar	**224.30**	**This study**	Ammonia-modified activated carbon	66.22	Ahmadfazelia *et al.* (2021)
	ABL@$ZnCl_2$	190.63	Li, P *et al.* (2023)	ZIF-8	30	Haghighat *et al.* (2023)
	ABL@H_3PO_4	184.70	Li, P *et al.* (2023)	Sugarcane bagasse biochar	23.61	Sun *et al.* (2018)
	Cassava slag biochar	105.3	Wu *et al.* (2020)	Rice bran biochar	21.33	Asgharzadeh *et al.* (2019)
	NaOH-treated rice husk	83.00	Khan & Shanableh (2022)	*Spirulina platensis* microalgae	20	Esmaili *et al.* (2023)
	Sulfur-doped biochar	33.10	Vigneshwaran *et al.* (2021)	Cu-ZIF-8	16	Haghighat *et al.* (2023)
	Fe–N biochar	12.14	Li, X *et al.* (2022)			

RhB, rhodamine B; MET, metronidazole; Fe–N biochar, iron–nitrogen biochar; ABL@$ZnCl_2$, zinc chloride functionalized *Atropa belladonna* L. biochar and ABL@H_3PO_4–H_3PO_4 functionalized *Atropa belladonna* L. biochar. (ZIF-8) – $C_8H_{10}N4$ Zn metal–organic frameworks, (Cu-ZIF-8) – $C_8H^{10}N_4ZnCu$ metal–organic frameworks.
Bold values represent results of this study.

temperature on the adsorption of RhB/MET can be explained as an effect of the energy of interaction between the adsorbates and the adsorbent as well as the kinetic energy of the molecules (Bello *et al.* 2019). At higher temperatures, the kinetic energy of the molecules increases, and this promotes desorption, leading to a lower adsorption capacity (Wu *et al.* 2020). RhB/MET and biochar interacted more strongly at 308 K than at 303 K, resulting in greater adsorption and higher percentage adsorption. Higher adsorption occurred at 308 K due to the adsorbate molecules possessing sufficient thermal energy to overcome the activation barrier and bind effectively to the adsorbent surface. The adsorption process at 330 K was further hindered by a reduced kinetic energy at lower temperatures. As the temperature increased from 308 to 313 K, the energy on interaction increased with an increase in kinetic energy, which encourages desorption and reduces adsorption (Sun *et al.* 2018).

The adsorption process was described using Langmuir, Freundlich, Temkin, and Dubinin–Radushkevich isotherm models (Figures S5a–h; supplementary document). The isotherm models specify the adsorbent affinity for RhB and MET, as well as the adsorption energetics and surface reactivity. A model's fitness is measured by its coefficient of determination (R^2) and error function (RMSE). For RhB at 303 K, Langmuir ($R^2 = 0.990$ and RMSE = 0.013) > Freundlich ($R^2 = 0.726$ and RMSE = 0.247) > Temkin ($R^2 = 0.636$ and RMSE = 0.491) > Dubinin–Radushkevich ($R^2 = 0.881$ and RMSE = 0.558) (Table 2). At 308 K, the order is Langmuir ($R^2 = 0.988$ and RMSE = 0.002) > Freundlich ($R^2 = 0.814$ and RMSE = 0.164) > Temkin ($R^2 = 0.555$ and RMSE = 0.393) > Dubinin–Radushkevich ($R^2 = 0.728$ and RMSE = 0.240) while at 313 K, the trend follows Langmuir ($R^2 = 0.991$ and RMSE = 0.001) > Freundlich ($R^2 = 0.812$ and RMSE = 0.163) > Temkin ($R^2 = 0.551$ and RMSE = 0.388) > Dubinin–Radushkevich ($R^2 = 0.722$ and RMSE = 0.241). Based on these results, the Langmuir isotherm described the adsorption of RhB on a homogenous monolayer surface of mesoporous biochar with the highest R^2 and the lowest RMSE at all temperatures and is the most suitable (Li *et al.* 2018, 2022, 2023; Azeez *et al.* 2020; Ren *et al.* 2020). For MET at 303 K, the most appropriate model follows Freundlich ($R^2 = 0.895$ and 0.394) > Langmuir ($R^2 = 0.691$ and RMSE = 4.476) > Temkin ($R^2 = 0.689$ and RMSE = 1.167) > Dubinin–Radushkevich ($R^2 = 0.610$ and RMSE = 1.461) while at 308 K, the model is ranked as Freundlich ($R^2 = 0.709$ and RMSE = 0.914) > Langmuir ($R^2 = 0.687$ and RMSE = 3.923) > Dubinin–Radushkevich ($R^2 = 0.450$ and RMSE = 1.724) > Temkin ($R^2 = 0.439$ and RMSE = 1.761) and at 313 K, Freundlich ($R^2 = 0.977$ and RMSE = 0.108) > Langmuir ($R^2 = 0.931$ and RMSE = 0.325) > Temkin ($R^2 = 0.897$ and RMSE = 0.349) > Dubinin–Radushkevich ($R^2 = 0.652$ and RMSE = 1.173) (Table 2). According to these results, the Freundlich isotherm was the most appropriate model for the adsorption of MET on heterogeneous mesoporous biochar. This was also the finding of Asgharzadeh *et al.* (2019), Li *et al.* (2022), and Esmaili *et al.* (2023).

The maximum monolayer adsorption capacities (q_{max}) for RhB were 31.181, 173.12, and 224.30 mgg^{-1} at 303, 308, and 313 K, increasing with temperature. For MET, the maximum monolayer adsorption capacities (q_{max}) were 95.44, 46.65, and 26.76 mgg^{-1} at 303, 308, and 313 K, respectively (Table 2). Adsorption capabilities for both adsorbates were affected by temperature. The highest temperature favoured RhB removal and the lowest temperature was suitable for MET. As previously reported, temperature has a significant influence on the adsorption of pollutants, so an increase would either increase or decrease their removal (Bello *et al.* 2019; Albanio *et al.* 2021). Based on these findings, it appears that temperature plays a significant role in increasing dye mobility on the mesoporous biochar surface through increased diffusion and intramolecular interactions. Biochar produced from palm trees for the removal of RhB and MET (Table 3) had significantly higher adsorption capacities than previously used biochar and some adsorbents for the removal of RhB and MET. This demonstrates that this adsorbent is a more promising option for dyes and pharmaceuticals removal given its adsorption capability, environmental friendliness, and ease of production. Both adsorbates have R_L values in the range of $0 < R_L < 1$, indicating a favourable adsorption process (Azeez *et al.* 2022). The Freundlich plot showed that the adsorption strength (n) was > 1 for both adsorbates at all temperatures, lending further support to the favourability of the adsorption process and physiosorption adsorption process (Liu *et al.* 2022). The K_f represents varied affinities of the adsorbent for RhB and MET at all temperatures and is proportional to the adsorption capacity (Bello *et al.* 2019; Vasseghian *et al.* 2022; Ghosh *et al.* 2023). In the Dubinin–Radushkevich plot, the adsorption energy (E) values ranged from 1.221 to 1.437 kJmol^{-1} for RhB and 1.061 to 1.107 kJmol^{-1} for MET, implying both adsorption processes were physisorption. Adsorption that occurs when $E > 8$ kJmol^{-1} is known as chemiosorption whereas when $E < 8$ kJmol^{-1}, it is physiosorption (Bonyadi *et al.* 2021; Azeez *et al.* 2023; Haghighat *et al.* 2023).

3.6. Influence of contact time on RhB and MET removal and adsorption kinetics

RhB and MET adsorption onto biochar was influenced by contact time, one of the most important variables in batch adsorption (Figure 5). The plot demonstrates that the adsorption capacity (q_t) rose with time reaching

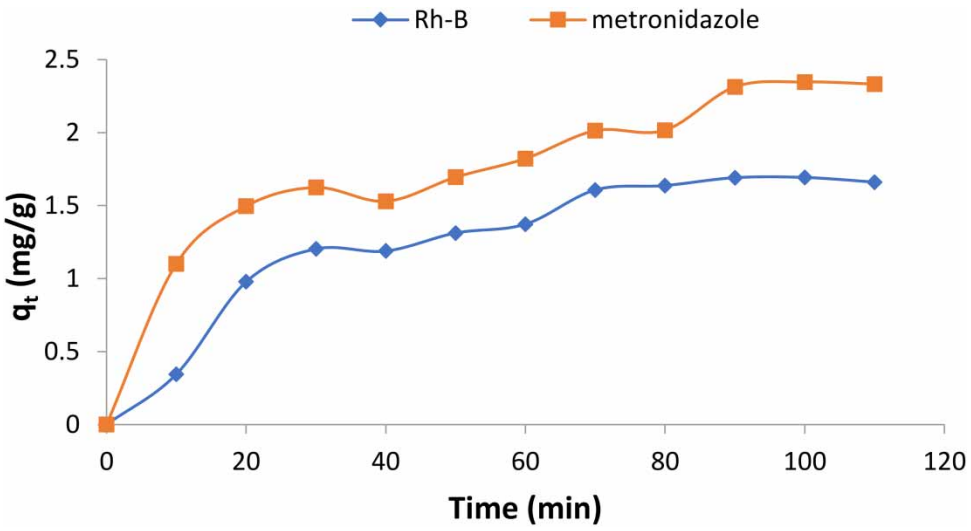

Figure 5 | Effect of contact time on the adsorption of RhB and MET on biochar.

equilibrium for MET at 100 min and RhB at 90 min. The increase in q_t of RhB rose from 0.34 mg/g at 10 min to 1.68 mg/g at 90 min at 303 K. As for MET, the value increased from 1.10 mg/g at 10 min to 2.39 mg/g at 100 min at 303 K. RhB/MET removal was initially rapid due to the availability of adsorptive sites on mesoporous biochar prior to equilibrium being reached when most of the sites were occupied (Bello *et al.* 2019; Bakry *et al.* 2022; Zhou *et al.* 2022).

RhB and MET removal kinetics and mechanisms were described using PFO, PSO, Elovich, and intra-particle diffusion equations. A model fitness estimate was determined by contrasting experimental and calculated q_e for PFO, PSO, and Elovich kinetics. Furthermore, the preferred model for describing adsorption kinetics is supported by a relatively lower χ^2 and higher coefficient of determination (R^2). The adsorption data for RhB and MET are best fitted to PSO kinetics with the highest R^2, lowest χ^2, and closest $q_{e_{experimental}}$ to $q_{e_{calculated}}$ (Table 4 and Figure S6 (supplementary document). In the studies carried out by Bonyadi *et al.* (2021), Elsayed *et al.* (2022), Li *et al.* (2022), Azeez *et al.* (2023) and Li *et al.* (2023), PSO was found to be the most effective kinetic method for the removal of RhB and MET. The mechanism governing the rate-determining step is a multilinear profile plots with three layers that did not pass through the origin in the intra-particle diffusion plot (Figure S7; supplementary document), suggesting that adsorption and intramolecular diffusion processes were also involved in the removal of RhB and MET (Li *et al.* 2022). RhB/MET diffusion from solution to biochar's surface was attributed to the significant increase in the first step, while intra-particle diffusion of RhB/MET was attributed to the considerable rise in the second step (Figure S7). A decrease in active sites on biochar may have resulted in a lower adsorption rate (K_{diff}) in the second step compared to the first. In the final stage, RhB/MET adsorbed onto the internal surface of the biochar, which is referred to as the equilibrium stage (Ren *et al.* 2020; Ghibate *et al.* 2021). Moreso, surface adsorption through the boundary layer (C) played a prominent role as well. The larger boundary layer could be the reason RhB adsorption was higher than MET (Ghibate *et al.* 2021).

3.7. Influence of temperature and adsorption thermodynamics

There was a temperature-dependent increase in RhB adsorption and a decrease in MET adsorption between 303 and 343 K (Figure 6). With an increase in temperature from 303 to 343 K, the RhB adsorption percentage increased from 47 to 87%, while the MET adsorption percentage decreased from 67 to 32%. For RhB, the adsorption trend with temperature indicates an endothermic adsorption process, whereas for MET, it suggests an exothermic process (Sun *et al.* 2018; Bello *et al.* 2019; Ren *et al.* 2020; Wu *et al.* 2020; Bonyadi *et al.* 2021; Ghibate *et al.* 2021; Bakry *et al.* 2022; Khan & Shanableh 2022; Li *et al.* 2022, 2023; Zhang *et al.* 2022; Azeez *et al.* 2023).

A description of the energetics and spontaneity involved in adsorption as determined by thermodynamic parameters in the Van't Hoff's plot (Figure S8; supplementary document) presents the values obtained for $\Delta G°$, $\Delta H°$,

Table 4 | Adsorption kinetics of RhB and MET on mesoporous biochar

$q_{e_{experiment}}$ (mg g^{-1})	Kinetic equations	Parameters	RhB 1.693	MET 2.347
Pseudo-first-order (PFO)	$\ln(q_e - q_t) = \ln q_e - K_1 t$	$q_{e_{calculated}}$ (mg g^{-1})	4.416	3.004
		K_1 (min^{-1})	0.063	0.032
		R^2	0.753	0.680
		χ^2	1.679	0.143
Pseudo-second-order (PSO)	$\frac{t}{q_t} = \frac{1}{K_2 q_e^2} + \frac{t}{q_e}$	$q_{e_{calculated}}$ (mg g^{-1})	2.078	2.801
		K_2 (g mg^{-1} min^{-1})	0.406	0.014
		R^2	0.919	0.967
		χ^2	0.071	0.073
Elovich	$q_t = \frac{1}{\beta}\ln(\alpha\beta) + \frac{1}{\beta}\ln t$	β (mg g^{-1} min^{-1})	2.156	1.954
		α (g mg^{-1})	0.156	0.383
		R^2	0.917	0.901
Intra-particle diffusion	$q_t = K_{diff} t^{1/2} + C$	K_{diff1}(mg g^{-1} min$^{-1/2}$)	0.376	0.230
		K_{diff2}(mg g^{-1} min$^{-1/2}$)	0.182	0.199
		K_{diff3}(mg g^{-1} min$^{-1/2}$)	0.054	0.046
		C_1 (mg g^{-1})	1.105	0.256
		C_2 (mg g^{-1})	0.824	0.781
		C_3 (mg g^{-1})	1.927	1.512
		R_1^2	0.964	0.956
		R_2^2	0.948	0.963
		R_3^2	0.226	0.715

RhB, rhodamine B; MET, metronidazole. q_t is the quantity of adsorbate adsorbed per unit time (mg g^{-1}), K_1, K_2, and K_{diff} are rate constants for the pseudo-first-order, pseudo-second-order, and intra-particle diffusion kinetic models, respectively. Elovich constant α represents the initial desorption rate while β is a desorption constant. R^2 and χ^2 are correlation coefficient and Chi-square, respectively.

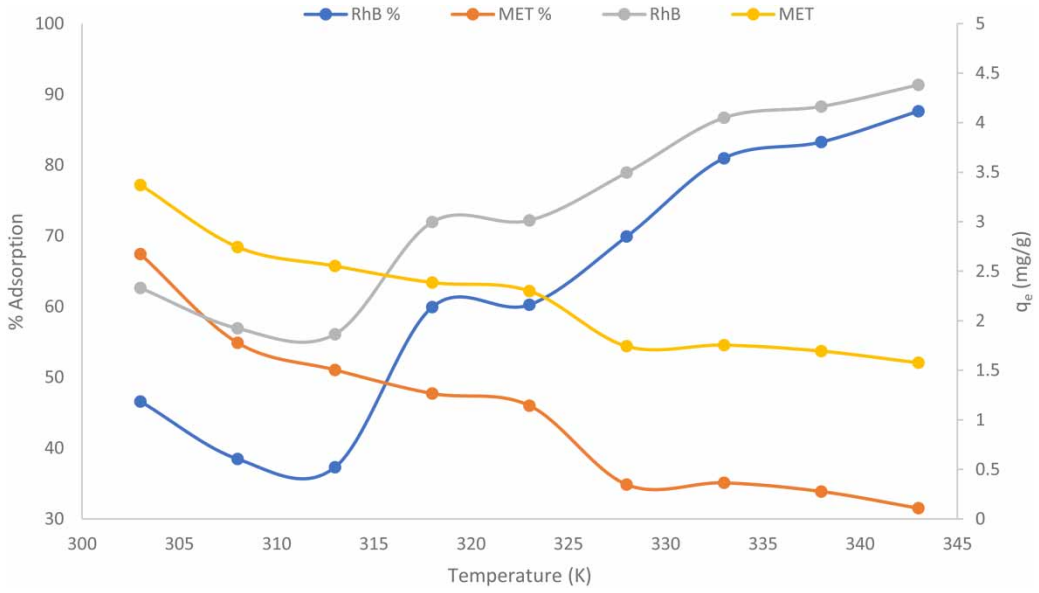

Figure 6 | Effect of temperature on the adsorption of RhB and MET on mesoporous biochar.

and $\Delta S°$ (Table 5). Positive values of $\Delta H°$ and $\Delta S°$ for RhB removal imply an endothermic process with a greater degree of randomness whereas for MET adsorption, both $\Delta H°$ and $\Delta S°$ were negative indicating an exothermic adsorption process with a decreased degree of randomness (Khan & Shanableh 2022; Zhang *et al.* 2022). The values of $\Delta G°$ ranged from -1.553 to -7.726 kJ mol^{-1} for RhB and from -19.385 to -17.938 kJ mol^{-1} for

Table 5 | Thermodynamic parameters of RhB and MET on mesoporous biochar

		RhB			MET		
Temperature (K)	Thermodynamic equations	$\Delta G°$ (kJ mol^{-1})	$\Delta H°$ (kJ mol^{-1})	$\Delta S°$ (J K^{-1} mol^{-1})	$\Delta G°$ (kJ mol^{-1})	$\Delta H°$ (kJ mol^{-1})	$\Delta S°$ (J K^{-1} mol^{-1})
303		−1.553			−19.385		
308		−2.325	45.206	154.32	−19.204	− 30.343	− 36.17
313		−3.097			−19.023		
318		−3.868			−18.843		
323		−4.640			−18.662		
328		−5.411			−18.481		
333		−6.183			−18.300		
338		−6.955			−18.119		
343		−7.726			−17.938		
	$\ln K_o = \frac{\Delta S°}{R} - \frac{\Delta H°}{RT}$						
	$\Delta G° = \Delta H° - T\Delta S°$						

RhB, rhodamine B; MET, metronidazole; R, gas constant (8.314 J mol^{-1}K^{-1}); T, temperature (K); $\Delta S°$, entropy change; $\Delta H°$, enthalpy change; $K_o = \frac{q_e}{C_e}$ and $\Delta G°$, change in free energy.

MET, indicating both adsorption processes were spontaneous at all temperatures with adsorption of RhB becoming more feasible with an increase in temperature while it became less feasible for MET as temperature increased (Li *et al.* 2023). The values of $\Delta H°$ obtained are +45.206 and −30.343 kJmol^{-1} for RhB and MET, respectively, confirming the physical adsorption processes for the removal of MET ($\Delta H° < 40$ kJmol^{-1}) and chemisorption for RhB ($\Delta H° > 40$ kJmol^{-1}) (Sun *et al.* 2018; Wu *et al.* 2020).

3.8. Reusability/regeneration

After four desorption studies, the percentage desorption bars of RhB-loaded biochar in water and ethanol (Figure S9a; supplementary document) demonstrate regeneration/desorption rates as high as 96 and 80% in water and ethanol, respectively. This suggests that water is a more effective solvent to desorb RhB. Better regeneration and higher desorption obtained for water could be due to its universal nature. Additionally, over 96% of RhB was removed after the fourth cycle, indicating better results than many previously reported adsorbents. Likewise, four desorption studies revealed that biochar loaded with MET can be regenerated/desorbed to as high as 95 and 69% in water and ethanol, respectively (Figure S9b; supplementary document). As the number of cycles increased, the reusability decreased for MET, but it was better than some previously reported adsorbents.

3.9. Proposed mechanism of RhB and MET adsorption on mesoporous biochar

Mesoporous biochar's cationic surface was electrostatically attracted to COO^- of RhB during RhB adsorption, followed by hydrogen bonding between OH and CO of the biochar and COOH and N^+ of RhB (Figure S10; supplementary document) (Haghighat *et al.* 2023). A similar mechanism has been proposed by Oladoye *et al.* (2022) for dye adsorption. Moreover, intramolecular and intra-particle diffusion played a role. The mechanism of MET adsorption was more prominent with electrostatic attraction and hydrogen bonding interaction between deprotonated MET and biochar (Figure S10) (Ghosh *et al.* 2023).

4. CONCLUSION

Palm tree biomass was successfully pyrolysed to produce biochar. The biochar produced contained functional groups O–H and C = O as revealed in the FTIR spectrum. The SEM micrograph also shows clustered images with EDXRF results showing the presence of carbon and other elements. Brunauer-Emmett-Teller suggests a type II isotherm with S_{BET} of 189.157 m^2 g^{-1} and pore diameter of 2.207 nm implying mesoporous nature. XRD spectrum shows six distinct peaks indicating high crystallinity that match JCPDS card number 00-712-6280. pH results show the mesoporous biochar has a cationic surface that interacted with COO^- of RhB and π–π ring of MET ring. Adsorption processes increased with an increase in biochar dosage and decreased with an increase in RhB/MET concentrations. Moreover, a decreased adsorption percentage was obtained for MET while an increase was obtained for RhB with an increase in temperature signifying exothermic and endothermic

adsorption processes, respectively. Based on coefficients of determination and root mean square error, Langmuir and Freundlich isotherms accurately described RhB and MET. RhB had its maximum adsorption capacity (q_{max}) ranged from 31.81 to 224.30 mg/g increasing with temperature and 95.44 to 26.76 mg/g for MET decreasing with temperature from 303 to 313 K. Other adsorption isotherm parameters indicate a favourable physiosorption process with pseudo-second-order kinetics as the most appropriate for both adsorbates. The adsorption process was spontaneous for both adsorbates as shown by $-\Delta G°$ following the endothermic process ($+\Delta H°$) for RhB removal and exothermic ($-\Delta H°$) for MET.

DATA AVAILABILITY STATEMENT

All relevant data are included in the paper or its Supplementary Information.

CONFLICT OF INTEREST

The authors declare there is no conflict.

REFERENCES

Adeniyi, A. G., Ighalo, J. O. & Onifade, D. V. 2019 Production of biochar from plantain (*Musa paradisiaca*) fibers using an updraft biomass gasifier with retort heating. *Combustion Science and Technology* **193**(1), 60–74. https://doi.org/10.1080/00102202.2019.1650269.

Ahmadfazelia, A., Poureshghb, Y., Rashtbarib, Y., Akbaria, H., Pouralib, P. & Adibzadeh, A. 2021 Removal of metronidazole antibiotic from aqueous solution by ammonia-modified activated carbon: Adsorption isotherm and kinetic study. *Journal of Water Sanitation & Hygiene for Development* **11**(6), 1083–1096. https://doi.org/10.2166/washdev.2021.117.

Akbari, H. & Adibzadeh, A. 2022 Persulphate activation under UV radiation for cyclophosphamide degradation and mineralisation in aqueous solution. *International Journal of Environmental and Analytical Chemistry* **102**(18), 1–14. https://doi.org/10.1080/03067319.2020.1817423.

Albanio, I. I., Muraro, P. C. L. & da Silva, W. L. 2021 Rhodamine B dye adsorption onto biochar from olive biomass waste. *Water, Air and Soil Pollution* **232**, 214. https://doi.org/10.1007/s11270-021-05110-6.

Asgari, E., Sheikhmohammadi, A. & Yeganeh, J. 2020 Application of the Fe_3O_4-chitosan nano-adsorbent for the adsorption of metronidazole from wastewater: Optimization, kinetic, thermodynamic and equilibrium studies. *International Journal of Biological Macromolecules* **164**, 694–706. https://doi.org/10.1016/j.ijbiomac.2020.07.188.

Asgharzadeh, F., Gholami, M., Jonidi, A., Kermani, M., Asgharnia, H. & Rezaeikalantary, R. 2019 Study of tetracycline and metronidazole adsorption on biochar prepared from rice bran kinetics, isotherms and mechanism. *Desalination and Water Treatment* **159**, 390–401. http://dx.doi.org/10.5004/dwt.2019.24140.

Azeez, L., Lateef, A., Adebisi, S. A. & Oyedeji, A. O. 2018 Novel biosynthesized silver nanoparticles from cobweb as adsorbent for rhodamine B: Equilibrium isotherm, kinetic and thermodynamic studies. *Applied Water Science* **8**, 32. https://doi.org/10.1007/s13201-018-0676-z.

Azeez, L., Lateef, A., Adejumo, A. L., Adeleke, T. A., Adetoro, R. O. & Mustapha, Z. 2020 Adsorption behaviour of rhodamine B on hen feather and corn starch functionalized with green synthesized silver nanoparticles (AgNPs) mediated with cocoa pods extracts. *Chemistry Africa* **3**, 237–250. https://doi.org/10.1007/s42250-019-00113-7.

Azeez, L., Adebisi, S. A., Adejumo, A. L., Busari, H. K., Aremu, H. K., Olabode, O. A. & Awolola, O. 2022 Adsorptive properties of rod-shaped silver nanoparticles-functionalized biogenic hydroxyapatite for remediating methylene blue and Congo red. *Inorganic Chemistry Communication* **142**, 109655. https://doi.org/10.1016/j.inoche.2022.109655.

Azeez, L., Adeleke, A. E., Popoola, S. A., Busari, H. K., Agbaje, W. B., Ojewuyi, S. S., Oluwafemi, I. I., Oladeji, R. D. & Adetoro, R. O. 2023 Dye degradation and molecular docking mechanism of *Terminalia catappa* mediated mesoporous titanium dioxide nanoparticles. *Inorganic Chemistry Communications* **153**, 110873. https://doi.org/10.1016/j.inoche.2023.110873.

Bakry, A., Darwish, M. S. A. & Hassanein, T. F. 2022 Adsorption of methylene blue from aqueous solutions using carboxyl/nitro-functionalized microparticles derived from polypropylene waste. *Iranian Polymer Journal* **31**(2), 185–197. https://doi.org/10.1007/s13726-021-00979-w.

Bello, O. S., Adegoke, K. A., Sarumi, O. O. & Lameed, O. S. 2019 Functionalized locust bean pod (*Parkia biglobosa*) activated carbon for rhodamine B dye removal. *Heliyon* **5**(8), e02323. https://doi.org/10.1016/j.heliyon.2019.e02323.

Bingül, Z. 2022 Determination of affecting parameters on removal of methylene blue dyestuff from aqueous solutions using natural clay: Isotherm, kinetic, and thermodynamic studies. *Journal of Molecular Structure* **1250**, 131729. https://doi.org/10.1016/j.molstruc.2021.131729.

Bonyadi, Z., Noghani, F., Dehghan, A., van der Hoek, J. P., Giannakoudakis, D. A., Ghadiri, S. K., Anastopoulos, I., Sarkhosh, M., Colmenares, J. C. & Shams, M. 2021 Biomass-derived porous aminated graphitic nanosheets for removal of the pharmaceutical metronidazole: Optimization of physicochemical features and exploration of process mechanisms. *Colloids and Surface A: Physicochemical and Engineering Aspects* **611**, 125791. https://doi.org/10.1016/j.colsurfa.2020.125791.

Burezq, H. & Davidson, M. K. 2023 Biochar from date palm (*Phoenix dactylifera* L.) residues – a critical review. *Arabian Journal of Geosciences* **16**(2). https://doi.org/10.1007/s12517-022-11123-0.

da Silva, W. L., Muraro, P. C. L., Pavoski, G., Espinosa, D. C. R. & dos Santos, J. H. Z. 2022 Preparation and characterization of biochar from cement waste for removal of rhodamine B dye. *Journal of Material Cycles & Waste Management* **24**, 1333–1342. https://doi.org/10.1007/s10163-022-01416-7.

Duan, X., Lv, R. & Kong, Z. 2020 An anionic metal-organic framework for selective adsorption separation toward methylene blue and rhodamine B. *Zeitschrift für Anorganische und Allgemeine Chemie* **646**(17), 1408–1411. https://doi.org/10.1002/zaac.202000264.

Elsayed, I., Madduri, S., El-Giar, E. M. & Hassan, E. 2022 Effective removal of anionic dyes from aqueous solutions by novel polyethylenimine-ozone oxidized hydrochar (PEI-OzHC) adsorbent. *Arabian Journal of Chemistry* **15**, 103757. https://doi.org/10.1016/j.arabjc.2022.103757.

Esmaili, Z., Barikbin, B., Shams, M., Alidadi, H., Al-Musawi, T. J. & Bonyadi, Z. 2023 Biosorption of metronidazole using *Spirulina platensis* microalgae: Process modeling, kinetic, thermodynamic, and isotherm studies. *Applied Water Science* **13**(2), 63. https://doi.org/10.1007/s13201-023-01867-9.

Ghibate, R., Senhaji, O. & Taouil, R. 2021 Kinetic and thermodynamic approaches on rhodamine B adsorption onto pomegranate peel. *Case Studies in Chemical and Environmental Engineering* **3**, 100078. https://doi.org/10.1016/j.cscee.2020.100078.

Ghosh, S., Falyouna, O., Onyeaka, H., Malloum, A., Bornman, C., AlKafaas, S. S., Al-Sharify, Z. T., Ahmadi, S., Dehghani, M. H., Mahvi, A. H. & Nasseri, S. 2023 Recent progress on the remediation of metronidazole antibiotic as emerging contaminant from water environments using sustainable adsorbents: A review. *Journal of Water Process Engineering* **51**, 103405. https://doi.org/10.1016/j.jwpe.2022.103405.

Haghighat, G. A., Gholikandi, G. B. & Mirabi, M. 2023 Removal of recalcitrant metronidazole from aqueous solution onto ZIF-8 & copper doped ZIF-8, process modelling and optimization. *International Journal of Environmental Analytical Chemistry* 1–19. https://doi.org/10.1080/03067319.2023.2185777.

Hanna, N., Sun, P., Sun, Q., Li, X., Yang, X., Ji, X., Zou, H., Ottoson, J., Nilsson, L. E., Berglund, B., Dyar, O. J., Tamhankar, A. J. & Lundborg, C. S. 2018 Presence of antibiotic residues in various environmental compartments of Shandong province in eastern China: Its potential for resistance development and ecological and human risk. *Environment International* **114**, 131–142. https://doi.org/10.1016/j.envint.2018.02.003.

Khan, M. I. & Shanableh, A. 2022 Adsorption of rhodamine B from an aqueous solution onto NaOH-treated rice husk. *Desalination and Water Treatment* **254**, 104–115. http://dx.doi.org/10.5004/dwt.2022.28356.

Le, P. T., Bui, H. T., Le, D. N., Nguyen, T. H., Pham, L. A., Nguyen, H. N., Nguyen, Q. S., Nguyen, T. P., Bich, N. T., Duong, T. T., Herrmann, M., Ouillon, S. & Le, T. P. Q. 2021 Synthesis, characteristics, and applications of novel nanomaterials in adsorption and catalysis. *Adsorption Science & Technology* 1–14. https://doi.org/10.1155/2021/9161904.

Li, Z., Potter, N., Rasmussen, J., Weng, J. & Lv, G. 2018 Removal of rhodamine 6G with different types of clay minerals. *Chemosphere* **202**, 127–135. https://doi.org/10.1016/j.chemosphere.2018.03.071.

Li, L., Tang, X., Li, W., Liang, S., Zhu, Q. & Wu, M. A. 2019 A case of methylprednisolone treatment for metronidazole-induced encephalopathy. *BMC Neurology* **19**(1), 49. https://doi.org/10.1186/s12883-019-1278-6.

Li, X., Shi, J. & Luo, X. 2022 Enhanced adsorption of rhodamine B from water by Fe-N co-modified biochar: Preparation, performance, mechanism and reusability. *Bioresource Technology* **343**, 126103. https://doi.org/10.1016/j.biortech.2021.126103.

Li, P., Zhao, T., Zhao, Z., Tang, H., Feng, W. & Zhang, Z. 2023 Biochar derived from Chinese herb medicine residues for rhodamine B dye adsorption. *ACS Omega* **8**(5), 4813–4825. https://doi.org/10.1021/acsomega.2c06968.

Liu, H., Wang, S., Gao, H., Yang, H., Wang, F., Chen, X., Fang, L., Tang, S., Yi, Z. & Li, D. 2022 A simple polyacrylamide gel route for the synthesis of $mgal_2o_4$ nanoparticles with different metal sources as an efficient adsorbent: Neural network algorithm simulation, equilibrium, kinetics and thermodynamic studies. *Separation and Purification Technology* **281**, 119855. https://doi.org/10.1016/j.seppur.2021.119855.

Mukherjee, A., Panda, B., Mondal, D., Mukherjee, D., Mukherjee, P., Sen, S., De, D., Dhak, P. & Dhak, D. 2023a Mesoporous, phase-pure Al^{3+} engrafted spinel $ZnAl_xb_{2-x}O_4$ $x = 0, 1$; $B = Cr^{3+}/Fe^{3+}$) for effective fluoride chemisorption and photodegradation of azo/non-azo dyes. *Journal of Environmental Chemical Engineering* **11**(1), 109237. https://doi.org/10.1016/j.jece.2022.109237.

Mukherjee, A., Dhak, P., Hazra, V., Goswami, N. & Dhak, D. 2023b Synthesis of mesoporous Fe/Al/La trimetallic oxide for photodegradation of various water-soluble dyes: Kinetic, mechanistic, and pH studies. *Environmental Research* **217**, 114862. https://doi.org/10.1016/j.envres.2022.114862.

Nasseh, N., Barikbin, B., Taghavi, L. & Nasseri, M. A. 2019 Adsorption of metronidazole antibiotic using a new magnetic nanocomposite from simulated wastewater (isotherm, kinetic and thermodynamic studies). *Composites Part B: Engineering* **159**, 146–156. https://doi.org/10.1016/j.compositesb.2018.09.034.

Nayak, A., Bhushan, B. & Kotnala, S. 2023 Evaluation of hydroxyapatite-chitosan-magnetite nanocomposites for separation of pharmaceuticals from water: A mechanistic and comparative approach. *Journal of Hazardous Material Advances* **10**, 100308. https://doi.org/10.1016/j.hazadv.2023.100308.

Oladoye, P. O., Bamigboye, M. O., Ogunbiyi, O. D. & Akano, M. T. 2022 Toxicity and decontamination strategies of Congo red dye. *Groundwater for Sustainable Development* **19**, 100844. https://doi.org/10.1016/j.gsd.2022.100844.

Olorunfemi, I. E., Komolafe, A. A., Fasinmirin, J. T. & Olufayo, A. A. 2019 Biomass carbon stocks of different land use management in the forest vegetative zone of Nigeria. *Acta Oecological* **95**, 45–56. https://doi.org/10.1016/j.actao.2019.01.004.

Ren, Z., Chen, F., Wang, B., Song, Z., Zhou, Z. & Ren, D. 2020 Magnetic biochar from alkali-activated rice straw for removal of rhodamine B from aqueous solution. *Environmental Engineering Research* **25**(4), 536–544. https://doi.org/10.4491/eer.2019.232.

Salem, I. B., Saleh, M. B., Iqbal, J., El Gamal, M. & Hameed, S. 2021 Date palm waste pyrolysis into biochar for carbon dioxide adsorption. *Energy Reports* **7**, 152–159. https://doi.org/10.1016/j.egyr.2021.06.027.

Sarkhosh, M., Sadani, M., Abtahi, M., Mohseni, S. M., Sheikhmohammadi, A., Azarpira, H., Najafpoor, A. A., Atafar, Z., Rezaei, S. & Alli, R. 2019 Enhancing photo-degradation of ciprofloxacin using simultaneous usage of e_{aq} and OH UV/ZnO/I^- process: Efficiency, kinetics, pathways, and mechanisms. *Journal of Hazardous Materials* **377**, 418–426. https://doi.org/10.1016/j.jhazmat.2019.05.090.

Sharma, J., Sharma, S., Bhatt, U. & Soni, V. 2022 Toxic effects of rhodamine B on antioxidant system and photosynthesis of *Hydrilla verticillate*. *Journal of Hazardous Materials Letters* **3**, 100069. https://doi.org/10.1016/j.hazl.2022.100069.

Sridhar, A., Ponnuchamy, M., Kapoor, A. & Prabhakar, S. 2022 Valorization of food waste as adsorbents for toxic dye removal from contaminated waters: A review. *Journal of Hazardous Materials* **424**, 127432. https://doi.org/10.1016/j.jhazmat.2021.127432.

Sun, L., Chen, D., Wan, S. & Yu, Z. 2018 Adsorption studies of dimetridazole and metronidazole onto biochar derived from sugarcane bagasse: Kinetic, equilibrium, and mechanisms. *Journal of Polymers and Environment* **26**, 765–777. https://doi.org/10.1007/s10924-017-0986-5.

Usman, M. A. & Khan, A. Y. 2022 Selective adsorption of anionic dye from wastewater using polyethyleneimine based macroporous sponge: Batch and continuous studies. *Journal of Hazardous Materials* **428**, 128238. https://doi.org/10.1016/j.jhazmat.2022.128238.

Vasseghian, Y., Dragoi, E. N. & Almomani, F. 2022 Graphene-based materials for metronidazole degradation: A comprehensive review. *Chemosphere* **286**, 131727. https://doi.org/10.1016/j.chemosphere.2021.131727.

Vigneshwaran, S., Sirajudheen, P., Karthikeyan, P. & Meenakshi, S. 2021 Fabrication of sulfur-doped biochar derived from tapioca peel waste with superior adsorption performance for the removal of Malachite green and rhodamine B dyes. *Surface and Interfaces* **23**, 100920. https://doi.org/10.1016/j.surfin.2020.100920.

Wu, J., Yang, J., Huang, G., Xu, C. & Lin, B. 2020 Hydrothermal carbonization synthesis of cassava slag biochar with excellent adsorption performance for rhodamine B. *Journal of Cleaner Production* **251**, 119717. https://doi.org/10.1016/j.jclepro.2019.119717.

Yaashikaaa, P. R., Kumar, P. S., Varjani, S. J. & Saravanan, A. 2019 Advances in production and application of biochar from lignocellulosic feedstocks for remediation of environmental pollutants. *Bioresource Technology* **292**, 122030. https://doi.org/10.1016/j.biortech.2019.122030.

Zhang, G., Lei, B., Chen, S., Xie, S. & Zhou, G. 2021 Activated carbon adsorbents with micro-mesoporous structure derived from waste *biomass* by stepwise activation for toluene removal from air. *Journal of Environmental Chemical Engineering* **9**(4), 105387. https://doi.org/10.1016/j.jece.2021.105387.

Zhang, X., Zhang, T., Guo, J., Ahmad, M., Yang, H., Su, X., Huang, F., Jin, Y., Xiao, H. & Song, J. 2022 Hierarchically porous tobacco midrib-based biochar prepared by a simple dual-templating approach for highly efficient rhodamine B removal. *Arabian Journal Chemistry* **15**, 103904. https://doi.org/10.1016/j.arabjc.2022.103904.

Zhou, Y., Li, Z., Ji, L., Wang, Z., Cai, L., Guo, J., Song, W., Wang, Y. & Piotrowski, A. M. 2022 Facile preparation of alveolate biochar derived from seaweed biomass with potential removal performance for cationic dye. *Journal of Molecular Liquid* **353**, 118623. https://doi.org/10.1016/j.molliq.2022.118623.

First received 14 August 2023; accepted in revised form 9 February 2024. Available online 2 March 2024